

# Entropy alternatives for equilibrium and out of equilibrium systems

Eugenio E. Vogel<sup>1,2</sup>, Francisco J. Peña<sup>3,\*</sup>, G. Saravia<sup>4</sup> and P. Vargas<sup>3</sup>

<sup>1</sup> *Departamento de Ciencias Físicas, Universidad de La Frontera, Casilla 54-D, Temuco 4811230, Chile*

<sup>2</sup> *Facultad de Ingeniería y Arquitectura, Universidad Central de Chile, Santiago 8330601, Chile*

<sup>3</sup> *Departamento de Física, Universidad Técnica Federico Santa María, 2390123 Valparaíso, Chile\* and*

<sup>4</sup> *Los Eucaliptus 1189, Temuco 4812537, Chile*

(Dated: April 4, 2025)

We introduce a novel entropy-related function, *non-repeatability*, designed to capture dynamical behaviors in complex systems. Its normalized form, *mutability*, has been previously applied in statistical physics as a dynamical entropy measure. To present the scope and advantages of these quantities, we analyze two distinct systems: (a) Monte Carlo simulations of magnetic moments on a square lattice and (b) seismic time series from the United States Geological Survey catalog. Both systems are well-established in the literature, serving as robust benchmarks. Shannon entropy is employed as a reference point to assess the similarities and differences with the proposed measures. A key distinction lies in the sensitivity of non-repeatability and mutability to the temporal ordering of data, which contrasts with traditional entropy definitions. Moreover, *sorted mutability*—the mutability computed from a reordered data version—reveals additional insights into the critical behavior of the systems under study.

## I. INTRODUCTION AND BACKGROUND

The notion of entropy was initially introduced by Clausius to formalize the second law of thermodynamics. He defined entropy ( $S(T)$ ) as a state function whose differential, for reversible processes, is given by:  $dS = \frac{\delta Q_{\text{rev}}}{T}$ , linking heat transfer to temperature and establishing a quantitative measure of irreversibility [1–6]. From a statistical perspective, entropy reflects the number of microscopic configurations compatible with a macroscopic state. This interpretation, pioneered by Boltzmann and later refined by Gibbs, bridges microscopic dynamics with macroscopic thermodynamic behavior. Based on energy microstates  $E_i$  and normalized probability  $p(E_i, T)$  of occupancy of such states, the energy is obtained by adding all the weighted contributions  $E(T) = \sum_i^{\text{all}} E_i p(E_i, T)$ . The partition function, which encapsulates the statistical properties of the system, is given by  $Z(T) = \sum_i^{\text{all}} e^{-E_i/k_B T}$ , with the Boltzmann constant  $k_B$ , which we take as 1.0, to measure energy in units of temperature.

Within the framework of Boltzmann-Gibbs statistics, the probability of occupying a microstate with energy  $E_i$  is given by  $p(E_i) = \frac{e^{-E_i/T}}{Z(T)}$ , which leads to the well-known expression for the thermodynamic entropy,

$$S(T) = - \sum_i p(E_i, T) \ln p(E_i, T). \quad (1)$$

This notion was later extended by Shannon [7] to quantify information in systems using a probabilistic description of their states. If the probability of the system being

in the  $i$ -th state at time  $t$  is  $p_i(t)$ , the Shannon entropy is defined as:

$$H(t) = - \sum_i p_i(t) \ln p_i(t), \quad (2)$$

where  $t$  is an independent variable characterizing the system's evolution or structure. Unlike  $S(T)$ , the probabilities  $p_i$  in Shannon's formulation are not necessarily derived from equilibrium statistical mechanics; rather, they may originate from empirical laws, intrinsic properties of the system, or even from direct measurements. In such cases, the probabilities can be estimated by sampling procedures. Specifically, in the present work, we obtain the probabilities  $p_i$  as relative frequencies, calculated as the ratio between the number of occurrences of the  $i$ -th state (frequency  $f_i$ ) and the total number of recorded observations  $R$ , that is,  $p_i = f_i/R$ .

The primary aim of this paper is to explore and compare a recently introduced normalized entropy measure, known as *mutability* [8], with the well-established Shannon entropy. As we will show, mutability contains Shannon entropy as a limiting, static case while also capturing essential information about the system's dynamics. This measure has been previously applied to a wide range of systems, including magnetic transitions [9–12], econophysical models [8, 13], nematic transitions [14, 15], wind energy systems [16, 17], hypertension datasets [18], seismic activity [19–24], and granular matter [25].

In this work, we aim to provide a more general presentation of mutability, focusing on its conceptual and quantitative relationship with Shannon entropy. Furthermore, we introduce the concept of *sorted mutability*, highlighting its differences from standard mutability and illustrating its application in distinct physical contexts.

Applications span both equilibrium and non-equilibrium systems, and we distinguish between

\* francisco.penar@usm.cl

artificial and natural systems. Here, we focus on two examples: (1) Monte Carlo (MC) simulations of spin systems and (2) seismic records from selected subduction zones. In most cases, the system's states and their associated probabilities are not fully known (except for small systems [11, 12]), and we rely instead on time series data sampled with finite precision, representing universes of varying dimensions.

We consider two representative spin systems: **1a)** The Ising model [26], describing short-range interacting magnetic moments in two dimensions. This model, known for its simplicity, is widely used as a benchmark for testing methodologies. **1b)** A dipolar interaction model [27], involving long-range interactions in 2D, which extends beyond the Ising framework. As we shall see, this difference leads to significant distinctions in the behavior of entropic measures.

For the case of seismicity, we analyze two highly active regions within the so-called “Ring of Fire,” the tectonically active subduction zone encircling the Pacific Ocean: **2a)** Southern California [28], where seismic activity poses significant risks to densely populated areas; and **2b)** a portion of the Alaskan seismic region [24, 29], which has recently experienced significant earthquake events.

This article is organized as follows. In the next section, we describe the systems under study, outline the methods, and present the theoretical background relevant to each case. Section III presents the results, accompanied by analysis and discussion. Section IV summarizes the main conclusions.

## II. SYSTEMS UNDER STUDY AND THEORETICAL BASIS

We begin by outlining the general features of the systems under study, describing their main characteristics. We consider two representative cases for each system and highlight the key differences in their respective modeling approaches.

**1) First System: Square Spin Lattice.** At a given temperature  $T$ , the system's energy  $E(T)$  is computed using the appropriate Hamiltonian, as detailed below. The time evolution is simulated via a Monte Carlo (MC) procedure in which, at each time step  $t$ , a spin (or magnetic moment) is randomly selected and temporarily flipped. The resulting energy difference  $\delta$  (defined as the energy before minus the energy after the flip) is evaluated. If  $\delta > 0$ , the flip is accepted unconditionally and  $E(t)$  is updated. If  $\delta < 0$ , the flip is accepted with a probability governed by the Metropolis criterion.

This process is carried out over  $20R$  MC steps at each temperature to ensure equilibration (with  $R$  defined per case). A subsequent sequence of  $20R$  MC steps is then used to collect data: every 20 MC steps, the value of a relevant observable is recorded, yielding a total of  $R$  entries. The most probable value of the observable is taken as its average over these  $R$  measurements. The

temperature is then updated as  $T_{i+1} = T_i + \Delta T$ , with  $\Delta T = 0.1$ , unless otherwise specified.

**1a) Ising Magnets.** In this case, the magnetic moments  $S_{jk}$  can take values  $+1$  (aligned with  $+y$ ) or  $-1$  (aligned with  $-y$ ). Only nearest-neighbor interactions are considered, described by the standard exchange Hamiltonian [30–32]:

$$H_X = -J \sum_{\langle jk, lm \rangle} \mathbf{S}_{jk} \cdot \mathbf{S}_{lm}, \quad (3)$$

where the summation is over all nearest-neighbor pairs, and  $J > 0$  denotes a ferromagnetic coupling constant. Indices  $(jk)$  and  $(lm)$  denote distinct lattice sites along the  $x$ - and  $y$ -directions respectively. Free boundary conditions are imposed, particularly suitable for modeling nanoscale systems [33].

**1b) Dipolar Magnets.** In this configuration, narrow ferromagnets with strong shape anisotropy are positioned at the vertices of the same square lattice and aligned along the  $y$ -axis. These magnets are treated as point dipoles, assuming their physical size is much smaller than the lattice spacing. Their interactions are mediated by the demagnetizing field, modeled via dipole-dipole interactions. The Hamiltonian contribution due to a dipole  $\mathbf{S}_{jk}$  interacting with all other dipoles  $\mathbf{S}_{lm}$  is given by [34]:

$$\Delta H_{D,jk} = \frac{\mu_0}{4\pi} \sum_{lm} \frac{\mathbf{S}_{jk} \cdot \mathbf{S}_{lm} - 3(\mathbf{S}_{jk} \cdot \hat{\mathbf{r}}_{jk,lm})(\mathbf{S}_{lm} \cdot \hat{\mathbf{r}}_{jk,lm})}{|\mathbf{r}_{jk,lm}|^3}, \quad (4)$$

where  $\mathbf{r}_{jk,lm}$  is the vector from site  $(jk)$  to  $(lm)$ , and  $\hat{\mathbf{r}}_{jk,lm}$  is its unit vector. The total Hamiltonian is obtained by summing over all dipole pairs (excluding self-interactions and double counting). The notation  $\mathbf{S}_{jk}$  is retained for consistency with the exchange model.

As shown in Fig. 1, the same lattice geometry is used for both the Ising (1a) and dipolar (1b) systems. In both cases, the total number of magnetic configurations is  $2^N$ , though the pathways by which

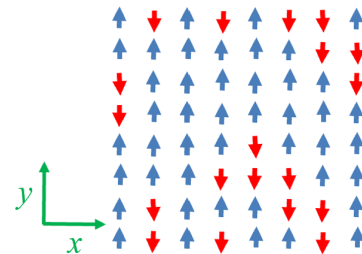


FIG. 1. Geometry of an  $8 \times 8$  lattice in the  $xy$ -plane. Magnetic moments can point upward or downward along the  $y$ -axis, corresponding to parallel or antiparallel orientations. These moments may represent Ising spins or highly anisotropic magnetic dipoles, treated as dimensionless quantities. Lattice sites are indexed by coordinates  $(jk)$ , with  $j = 1, 2, \dots, L$  along the  $x$ -axis and  $k = 1, 2, \dots, L$  along the  $y$ -axis.

these states are accessed—e.g., by increasing temperature—differ markedly.

An essential advantage of the information-theoretic approach is that it identifies states based on matching significant digits of numerical observables. Since only relative values are needed, we adopt  $J = 1$  for the Ising case and set  $\mu_0/4\pi = 1$  and the lattice spacing to unity in the dipolar case. This simplifies the simulations while preserving the relevant dynamical structure of the system. We present the Monte Carlo (MC) simulation results exclusively for the cases of pure exchange and pure dipolar interactions. Under the above conditions, the transition temperatures are comparable in both cases.

**2) Second System: Seismic Activity.** The United States Geological Survey (USGS) provides a comprehensive catalog of seismic events in the United States [35]. From this database, we extract a time series of earthquake magnitudes exceeding a given threshold (typically Mw 1.5) within a predefined geographical "rectangle" and depth range. Two specific regions are considered:

**2a) California Seismicity.** Data is selected from the region bounded by longitudes 115°W to 119°W and latitudes 31°N to 35°N, with depths limited to 35 km. The data extraction covers the period from January 1, 1994, to December 31, 2023, yielding a total of 131,459 seismic events. This region includes the Mw 7.2 El Mayor–Cucapah earthquake of April 4, 2010.

**2b) Alaska Seismicity.** Data is extracted from a smaller region defined by longitudes 157.3°W to 158.2°W and latitudes 54.5°N to 55.5°N, down to depths of 70 km. The time span from January 1, 2020, to December 31, 2023, includes 629 recorded earthquakes. This region is notable for recent intense seismic activity, including the Mw 8.2 Chignik earthquake of July 29, 2021. Due to the relatively low number of events, this dataset provides an opportunity to test information-theoretic methods under sparse-data conditions.

To illustrate the application of these methods, we analyze a subset of 32 earthquakes from the California dataset occurring close to the Mw 5.3 event on June 5, 2021. The magnitudes (rounded to one decimal place) are listed in Table I.

**Mutability.** Let  $Q(t)$  denote a time-ordered sequence of an observable  $Q$  (or, more generally, any parameter-indexed sequence), such as the one shown in the second column of Table I. Although the table is based on seismic magnitude data, the methodology is not restricted to this context. It may be applied to other types of sequences, including physical properties of magnetic systems (e.g., energy or magnetization), fluid vorticity, components along a DNA molecule, or any order parameter of interest.

We now consider a segment of  $R$  registers of the sequence  $Q(t)$ , ending at time  $t$ . The weight in bytes of this segment is denoted by  $w(Q, R, t)$ . Applying the compressor `wlzip` [22] to this segment yields a symbolic representation (third column in Table I) whose size is denoted by

TABLE I. Segment of a seismic dataset retrieved from the USGS, consisting of  $R = 32$  consecutive earthquake events. The columns are: (1) event index  $i$ , (2) earthquake magnitudes  $M_W$  (weight  $w$ ), (3) compressed symbolic map of  $M_W$  (weight  $w^*$ , using `wlzip`), (4) frequency  $f_i$ , (5) probability  $p_i = f_i/R$ , (6) sorted magnitudes  $SM_W$  (weight  $w$ ), and (7) symbolic map of the sorted magnitudes (compressed with weight  $w^\dagger$ ). Mutability values  $\zeta$  are shown in the last row.

$i$	$M_W$	Map of $M_W$	$f_i$	$p_i$	$SM_W$	Map of $SM_W$
1	1.7	1.7 0 10 12 9	4	0.12500	1.5	1.5 0,2
2	2.7	2.7 1	1	0.03125	1.5	1.6 2,4
3	1.5	1.5 2,2	2	0.06250	1.6	1.7 7,4
4	1.5	1.8 4	1	0.03125	1.6	1.8 11
5	1.8	1.6 5 2 2 4,2	5	0.15625	1.6	1.9 ; 12,3
6	1.6	2.4 8 15 3	3	0.09375	1.6	2.0 15
7	1.9	2.0 11	1	0.03125	1.6	2.2 16,3
8	1.6	2.2 12 9 9	3	0.09375	1.7	2.3 19
9	2.4	3.9 15 2	2	0.06250	1.7	2.4 20,3
10	1.6	5.4 16	1	0.03125	1.7	2.6 23,2
11	1.7	2.9 18,2	2	0.06250	1.7	2.7 25
12	2.0	1.9 6 18 5	3	0.09375	1.8	2.9 26,2
13	2.2	2.6 20 8	2	0.06250	1.9	3.4 28
14	1.6	3.4 25	1	0.03125	1.9	3.9 29,2
15	1.6	2.3 27	1	0.03125	1.9	5.4 31
16	3.9				2.0	
17	5.4				2.2	
18	3.9				2.2	
19	2.9				2.2	
20	2.9				2.3	
21	2.6				2.4	
22	2.2				2.4	
23	1.7				2.4	
24	2.4				2.6	
25	1.9				2.6	
26	3.4				2.7	
27	2.4				2.9	
28	2.3				2.9	
29	2.6				3.4	
30	1.9				3.9	
31	2.2				3.9	
32	1.7				5.4	
$\zeta$	1.0	0.944				0.594

$w^*(Q, R)$ . This compressed map is generated by traversing the original file (second column), opening a new row in the third column for each newly encountered value. This value is written at the beginning of the row, followed by its distance (in number of positions) from the first register in the file. The map records the distance to the previous appearance of the same value for repeated appearances, and the number of consecutive repetitions is denoted after a comma. Refs. [17, 22] provides a detailed description of the algorithm. No information is lost in the process, as an inverse algorithm can reconstruct the original sequence  $Q(t)$ .

The regular mutability associated with this file is then defined as [11, 12, 14, 16, 19, 20]:

$$\zeta(Q, R, t) = \frac{w^*(Q, R)}{w(Q, R, t)}. \quad (5)$$

An alternative informational analysis can be performed by first sorting the data sequence in ascending (or descending) order by magnitude. This reordering does not affect the physical meaning of the observables but provides insight into the underlying data structure. The sixth column of Table I contains the same values as the second, but sorted. The corresponding symbolic repre-

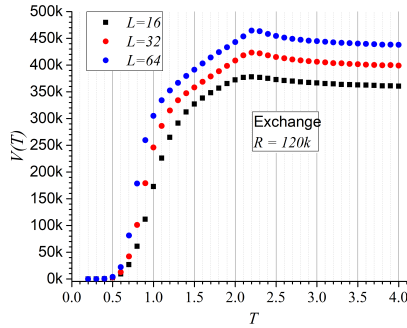


FIG. 2. Average computational entropy  $V(T)$  for exchange interaction only as a function of temperature  $T$ , for three different lattice sizes. The factor  $k$  corresponds to  $10^3$ .

sensation using **wlzip**, constructed identically as before, is presented in the seventh column with weight  $w^\dagger$ . The mutability of this sorted sequence (hereafter referred to as \*sorted mutability\*) is defined as:

$$\zeta_S(Q, R, t) = \frac{w^\dagger(Q, R)}{w(Q, R, t)}. \quad (6)$$

By construction, the sorted mutability  $\zeta_S$  provides a lower bound for mutability, thus enhancing the identification of critical points, as shown in the results below.

In principle, any data compression algorithm can be employed to analyze the informational content of a sequence. However, most widely available compressors on the web are designed to recognize digit patterns independently of their position, which may be efficient for general data compression but fails to retain the structural properties of the sequence. Early studies employed **bzip2** to obtain mutability results. Nevertheless, unexpected overlaps between results of systems with different sizes [9] motivated the development of a state-oriented compressor, **wlzip** ("word length zipper") [10]. Although **wlzip** typically compresses less efficiently than **bzip2**, **rar**, or other general-purpose compressors, it is explicitly designed to preserve state-related structure. Thus, using **wlzip** or similar state-aware compressors is essential for a meaningful definition of mutability.

**Functions.** For each system and observable  $Q$ , we report four functions:

- i) *Non-repeatability*  $V$ , defined directly by the compressed weight:  $V = w^*(Q, R)$ ;
- ii) *Regular mutability*  $\zeta$ , given by Eq. (5);
- iii) *Sorted mutability*  $\zeta_S$ , given by Eq. (6);
- iv) *Shannon entropy*  $H$ , given by Eq. 2.

The probabilities  $p_i$ , shown in the fifth column of Table I, are readily provided by **wlzip**. Therefore, the process of obtaining mutability as normalized repeatability

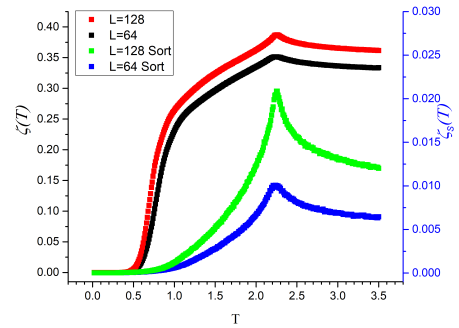


FIG. 3. Mutability for Ising systems of lattice sizes  $L = 64$  and  $L = 128$ . The two upper curves correspond to regular mutability, while the two lower curves correspond to sorted mutability for the same original data.

*inherently produces the Shannon entropy  $H$  as a special case.*

The regular mutability  $\zeta$  has been applied in various fields [15, 17, 22, 25] and can be interpreted as a form of dynamical entropy closely related to the classical Shannon entropy. In this work, we compare mutability with the other quantities introduced above, especially the non-repeatability  $V$ . Furthermore, we show that sorted mutability  $\zeta_S$  provides additional structural insight into the data sequence and is particularly relevant near critical conditions.

In recent studies, mutability has been compared with Tsallis entropy in the context of seismic data. It was found that the two measures provide complementary perspectives [22, 24, 36, 37]. However, we do not include Tsallis entropy in the present analysis for two main reasons: (i) Simplicity of presentation, to focus on the relationship between classical Shannon entropy and the more recent mutability function; and (ii) Relevance to the systems under study since the magnetic simulations are based on the Metropolis Monte Carlo algorithm, which adheres to Boltzmann statistics. In this context, Tsallis entropy is not expected to capture the finer features of data sequences derived from these simulations.

### III. RESULTS AND DISCUSSION

Figure 2 presents the non-repeatability results for a data sequence corresponding to a spin lattice with exchange interactions. We consider  $R = 1.2 \times 10^5$  records. As the observation window increases (i.e., larger  $R$ ), the differences between results for different lattice sizes become more evident. However, obtaining precise proportions would require not only larger samples but also larger lattice sizes (to minimize boundary effects) and a broader temperature range, which lies beyond the scope of the present article.

Figure 3 displays both regular mutability (upper

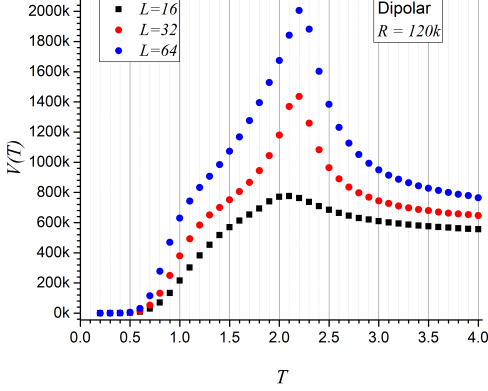


FIG. 4. Average computational entropy  $V(T)$  for the dipolar interaction only, as a function of temperature  $T$ , for three different lattice sizes.  $k$  indicates a factor of 1000.

curves) and sorted mutability (lower curves) for Ising systems with  $L = 64$  and  $L = 128$ . The regular mutability exhibits the typical shape of an entropy curve as a function of temperature: starting at zero, increasing gently, then more sharply, and finally saturating. Notably, the curve presents a maximum around  $T \approx 2.7$ , which corresponds to the well-known critical temperature of the two-dimensional Ising model [38].

In contrast, the sorted mutability reveals a single, well-defined peak at the critical temperature, suggesting it is a particularly effective indicator of critical behavior. Furthermore, the sharpness of this peak increases with system size, reinforcing its usefulness.

We now turn to the second magnetic system, governed by dipolar interactions. Figure 4 shows the non-repeatability function for three lattice sizes. The data confirm the ordering  $V_{L=16}(T) < V_{L=32}(T) < V_{L=64}(T)$ . With sample sizes exceeding  $1.2 \times 10^5$  records and larger lattices, the tendency to reach higher values of non-repeatability is maintained. The maxima become more pronounced and shift slightly toward higher critical temperatures as the system size increases, approaching the

well-known critical temperature  $T_C = 2.27$ , similar to the case with exchange interactions. This agreement arises from setting the magnitude scaling factors to unity in both cases.

In the left panel of Fig. 5, we compare Shannon entropy, regular mutability, and sorted mutability for  $L = 32$ , using  $R = 4.8 \times 10^5$  records (corresponding to  $9.6 \times 10^6$  Monte Carlo steps, with an equal number of equilibration steps). We selected the dipolar system for this comparison due to its less monotonic behavior with temperature. Although the plots use different scales, the vertical ranges have been normalized for comparability.

As noted from Table I, Shannon entropy is intrinsically linked to mutability, and sorted mutability is derived from the same symbolic compression scheme. Consequently, all three quantities follow a similar qualitative trend: starting at zero, growing with temperature, reaching a peak at the critical point, and then decreasing toward higher temperatures. However, their specific temperature dependence reveals distinct sensitivities. In particular, sorted mutability displays the sharpest peak at the critical temperature, indicating it is the most precise among the three in identifying phase transitions.

The right panel of Fig. 5 shows regular mutability for the same system and parameters but for varying observation window sizes  $R$ , as specified in the inset. The lowest curve in the right panel corresponds to the same regular mutability curve (in black) shown on the left. The figure demonstrates that the curves coincide at low temperatures but diverge near the critical region. As  $R$  increases, the maximum mutability value decreases and the curves flatten out at high temperatures. This behavior is expected to continue until it converges to the classical entropy curve in the thermodynamic limit: a mildly increasing curve with an inflection point and eventual saturation at high temperatures.

Therefore, the peak in mutability seen in Fig. 5 is a finite-size effect due to the limited observation window. Nonetheless, this feature can be advantageous for locating critical points: by tuning the observation window  $R$ , one can efficiently estimate  $T_C$  within practical computational timescales, depending on the system under investigation.

We now turn our attention to seismic activity, beginning with the Los Angeles/San Diego region in California. Figure 6 shows the Shannon entropy, mutability, and sorted mutability for overlapping time windows of  $r = 128$  consecutive events (with an overlap of one event). Here,  $r$  denotes the number of records used for information processing, which is significantly smaller than the values of  $R$  used for the magnetic system simulations. The aim is to explore whether small but significant variations can be detected in natural systems, where the number of data entries is limited—first by nature and second by the sensitivity of measurement instruments.

The vertical axes have been adjusted so that all three curves span approximately the same maximum range (about 0.65 units on the left axis, measured between the

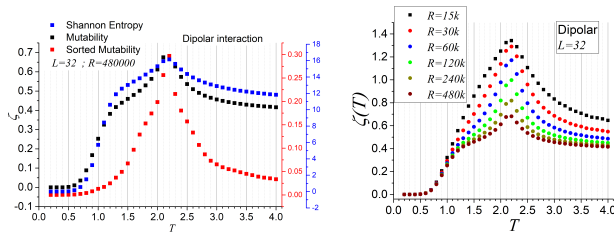


FIG. 5. Left: Shannon entropy, regular mutability, and sorted mutability for  $L = 32$ , computed over 480,000 registers. Right: Regular mutability for  $L = 32$  with different observation window sizes  $R$ , as indicated in the inset.  $k$  denotes a factor of 1000.



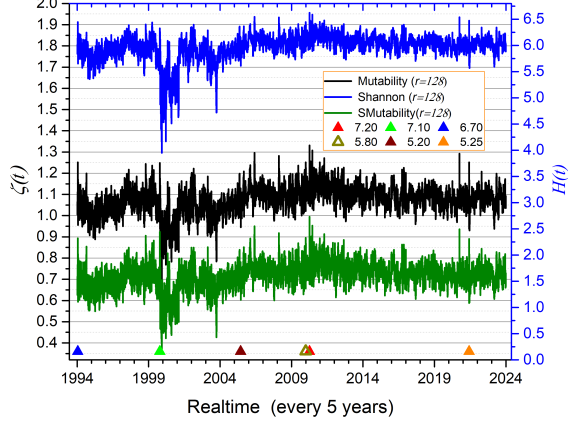


FIG. 6. Shannon entropy, mutability, and sorted mutability for 131,459 earthquakes recorded between 1994 and 2023, with magnitudes  $M_w \geq 1.5$ , depths up to 30 km, and epicenters located within the rectangular region around Los Angeles and San Diego, as defined in the text. The occurrence times of major earthquakes are marked by symbols described in the inset.

2012 maximum and the corresponding minimum around 2000).

Several observations follow:

1. The similarity of the three curves confirms the connection between Shannon entropy and mutability.
2. Major earthquakes tend to coincide with upward spikes in the curves; however, the converse is not always true—some spikes are not linked to single large events, indicating the possible influence of local activity or seismic swarms.
3. Mutability curves more clearly reveal the undulating trends in the data.
4. Downward behavior associated with aftershock regimes is better captured by mutability curves.
5. Mutability exhibits richer texture than Shannon entropy, with greater amplitude and clearer resolution of consecutive segments.
6. Sorted mutability provides slightly more detail than regular mutability—for example, the downward triplet near 1995, sharper peaks around 2010, and broader oscillation ranges within the same vertical span.

The case of the Alaska earthquake of magnitude  $M_w = 8.2$  in 2021 is quite different, as seismic activity in this region is sparse. The dataset for the rectangular zone bounded by  $54.5\text{--}55.5^\circ\text{N}$  and  $157.3\text{--}158.2^\circ\text{W}$  consists of only 629 events recorded over 24 years. This case is included to test the method under extreme data scarcity, in order to verify whether the features observed in the California analysis still hold. It is known that seismic frequency decreases in the lead-up to major earthquakes, a pattern previously identified in this same region [24].

For this analysis, the geographic region was intentionally narrowed to accentuate data scarcity. Although the earthquake catalog begins in 2000, the plots in Fig. 7 start in 2012, when the first set of 64 events became avail-

able for computing mutability. Shannon entropy plots were excluded from this figure, as they offer no additional information beyond what is captured by regular and sorted mutability.

The upper panel of Fig. 7 presents the regular mutability for this sequence of 629 magnitudes, using overlapping windows of  $r = 64$  events. The initial mutability values are below 850. Around the end of 2016, mutability increases stepwise to approximately 900, reflecting a period of variable seismic activity. In early 2019, a drop in mutability indicates repetitive values characteristic of a quiescent phase. The mutability then oscillates until the  $M_w = 8.2$  earthquake of 2021 enters the 64-event window, producing a marked spike due to the extreme diversity of values. This is followed by a sharp drop (a downward spike), signaling the onset of the aftershock regime. After a brief recovery, another smaller dip occurs, reflecting continued energy relaxation. By the end of 2023, mutability drops to low values, due to the occurrence of several moderate earthquakes in or near the selected region, sustaining a moderate aftershock phase. In this context, low mutability may indicate ongoing energy dissipation, potentially reducing the likelihood of an imminent large event.

The lower panel of Fig. 7 shows sorted mutability computed with the same parameters. Comparison with regular mutability reveals several key points:

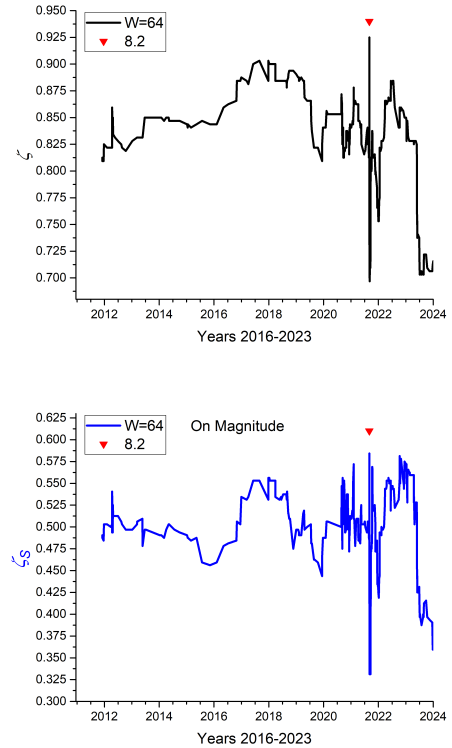


FIG. 7. Mutability analysis of seismic data in the Alaska region. Top: Regular mutability. Bottom: Sorted mutability.

1. Sorted mutability values are lower than regular mutability, consistent with previous observations in magnetic systems. 2. The major features of the regular mutability curve—especially the spikes associated with the 2021 event and its aftermath—are clearly preserved. 3. General trends and curvature are more pronounced in the sorted mutability plot. 4. The texture of the sorted mutability curve is richer; notably, oscillations starting at the end of 2020 (potential precursors to the main shock?) exceed the 2017–2018 maxima.

These results confirm the utility of mutability-based measures, even in data-limited natural systems.

#### IV. CONCLUSIONS

The non-repeatability function  $V(T)$  increases with system size (i.e., the number of elements in the lattice), suggesting a possible tendency toward additivity. However, this behavior is not yet fully resolved due to finite equilibration and observation times. This trend is observed in both exchange and dipolar interaction systems, though it is more pronounced in the latter. The enhanced effect for dipolar systems is likely due to their richer dynamics and the influence of long-range interactions, which allow broader sampling in configuration space.

Mutability incorporates Shannon entropy as a special case, particularly when the symbolic mapping produced by the `wlzip` compressor corresponds directly to the frequency of states. This relationship is confirmed by the observation that mutability curves consistently lie below the Shannon entropy curves in spin systems, enabling a

clearer identification of critical points. Notably, the maxima observed in mutability near the critical temperature are artifacts arising from finite observation times.

Sorted mutability produces sharper peaks at critical points compared to regular mutability, making it a valuable tool for detecting phase transitions. This measure can be tuned by adjusting the system size and the sampling window, offering flexibility and precision in the analysis of complex systems.

In the context of seismic activity, both mutability and Shannon entropy effectively characterize temporal patterns. Upward spikes in Fig. 6 correspond to either major earthquakes or clusters of moderate events (swarms), while low values are typically associated with aftershock regimes characterized by repeated low-magnitude events. Additionally, low mutability values may reflect continuous energy release via moderate events in highly active regions.

Sorted mutability provides a more refined view of criticality, both in spin systems and, to a certain extent, in seismic data. It offers enhanced texture, a better definition of temporal structures, and more pronounced contrast in identifying key dynamical features.

In summary, regular mutability—and even more so, sorted mutability—offers significant advantages over Shannon entropy. Sorted mutability reveals deeper structure in data sequences, captures oscillatory trends with enhanced clarity, and offers more sensitive detection of aftershock sequences and phase transitions.

#### ACKNOWLEDGEMENTS

Authors acknowledge partial support from ANID Fondecyt Grant (Chile) under contracts 1230055 and 1240582.

- 
- [1] C. Tsallis, Entropy, Encyclopedia **2**, 264 (2022).
  - [2] A. Wehrl, General properties of entropy, Reviews of Modern Physics **50**, 221 (1978).
  - [3] W. Greiner, L. Neise, and H. Stöcker, *Thermodynamics and statistical mechanics* (Springer Science & Business Media, 2012).
  - [4] H. B. Callen and H. Scott, Thermodynamics and an introduction to thermostatistics (1998).
  - [5] E. Zanchini and G. P. Beretta, Recent progress in the definition of thermodynamic entropy, Entropy **16**, 1547 (2014).
  - [6] E. P. Gyftopoulos *et al.*, Entropy: Thermodynamic definition and quantum expression, Physical Review E **55**, 3851 (1997).
  - [7] C. E. Shannon, A mathematical theory of communication, The Bell system technical journal **27**, 379 (1948).
  - [8] E. E. Vogel and G. Saravia, Information theory applied to econophysics: stock market behaviors, The European Physical Journal B **87**, 1 (2014).
  - [9] E. Vogel, G. Saravia, and L. Cortez, Data compressor designed to improve recognition of magnetic phases, Physica A: Statistical Mechanics and its Applications **391**, 1591 (2012).
  - [10] V. Cortez, G. Saravia, and E. Vogel, Phase diagram and reentrance for the 3d edwards–anderson model using information theory, Journal of magnetism and magnetic materials **372**, 173 (2014).
  - [11] O. A. Negrete, P. Vargas, F. J. Peña, G. Saravia, and E. E. Vogel, Entropy and mutability for the q-state clock model in small systems, Entropy **20**, 933 (2018).
  - [12] O. A. Negrete, P. Vargas, F. J. Peña, G. Saravia, and E. E. Vogel, Short-range berezinskii-kosterlitz-thouless phase characterization for the q-state clock model, Entropy **23**, 1019 (2021).
  - [13] E. Vogel, G. Saravia, J. Astete, J. Díaz, and F. Riadi, Information theory as a tool to improve individual pensions: The Chilean case, Physica A: Statistical Mechanics and its Applications **424**, 372 (2015).
  - [14] E. Vogel, G. Saravia, and A. J. Ramirez-Pastor, Phase transitions in a system of long rods on two-dimensional lattices by means of information theory, Physical Review E **96**, 062133 (2017).

- [15] E. Vogel, G. Saravia, A. J. Ramirez-Pastor, and M. Pasinetti, Alternative characterization of the nematic transition in deposition of rods on two-dimensional lattices, *Physical Review E* **101**, 022104 (2020).
- [16] E. Vogel, G. Saravia, S. Kobe, R. Schumann, and R. Schuster, A novel method to optimize electricity generation from wind energy, *Renewable Energy* **126**, 724 (2018).
- [17] E. Vogel, G. Saravia, S. Kobe, and R. Schuster, Onshore versus offshore capacity factor and reliability for wind energy production in germany: 2010–2022, *Energy Science & Engineering* **12**, 2198 (2024).
- [18] D. J. Contreras, E. E. Vogel, G. Saravia, and B. Stockins, Derivation of a measure of systolic blood pressure mutability: A novel information theory-based metric from ambulatory blood pressure tests, *Journal of the American Society of Hypertension* **10**, 217 (2016).
- [19] E. Vogel, G. Saravia, D. Pastén, and V. Muñoz, Time-series analysis of earthquake sequences by means of information recognizer, *Tectonophysics* **712**, 723 (2017).
- [20] E. E. Vogel, F. G. Brevis, D. Pastén, V. Muñoz, R. A. Miranda, and A. C.-L. Chian, Measuring the seismic risk along the nazca–south american subduction front: Shannon entropy and mutability, *Natural Hazards and Earth System Sciences* **20**, 2943 (2020).
- [21] D. Pasten, G. Saravia, E. E. Vogel, and A. Posadas, Information theory and earthquakes: depth propagation seismicity in northern chile, *Chaos, Solitons & Fractals* **165**, 112874 (2022).
- [22] D. Pasten, E. E. Vogel, G. Saravia, A. Posadas, and O. Sotolongo, Tsallis entropy and mutability to characterize seismic sequences: The case of 2007–2014 northern chile earthquakes, *Entropy* **25**, 1417 (2023).
- [23] A. Posadas, D. Pasten, E. E. Vogel, and G. Saravia, Earthquake hazard characterization by using entropy: Application to northern chilean earthquakes, *Natural Hazards and Earth System Sciences* **23**, 1911 (2023).
- [24] E. E. Vogel, D. Pastén, G. Saravia, M. Aguilera, and A. Posadas, 2021 alaska earthquake: entropy approach to its precursors and aftershock regimes, *Natural Hazards and Earth System Sciences* **24**, 3895 (2024).
- [25] R. Caitano, A. Ramirez-Pastor, E. Vogel, and G. Saravia, Competition analysis of grain flow versus clogging by means of information theory, *Granular Matter* **26**, 77 (2024).
- [26] E. Ising, *Beitrag zur theorie des ferro-und paramagnetismus*, Ph.D. thesis, Grefe & Tiedemann Hamburg, Germany (1924).
- [27] A. MacIsaac, A model magnetic thin film with dipolar and exchange interactions, *Physica A: Statistical Mechanics and its Applications* **239**, 147 (1997).
- [28] A. Bostrom, S. K. McBride, J. S. Becker, J. D. Goltz, R.-M. de Groot, L. Peek, B. Terbush, and M. Dixon, Great expectations for earthquake early warnings on the united states west coast, *International Journal of Disaster Risk Reduction* **82**, 103296 (2022).
- [29] R. Qu, Y. Ji, W. Zhu, Y. Zhao, and Y. Zhu, Fast and slow earthquakes in alaska: Implications from a three-dimensional thermal regime and slab metamorphism, *Applied Sciences* **12**, 11139 (2022).
- [30] G. F. Newell and E. W. Montroll, On the theory of the ising model of ferromagnetism, *Reviews of Modern Physics* **25**, 353 (1953).
- [31] H. J. Zandvliet and C. Hoede, Spontaneous magnetization of the square 2d ising lattice with nearest-and weak next-nearest-neighbour interactions, *Phase Transitions* **82**, 191 (2009).
- [32] J. Dixon, J. Tuszynski, and E. Carpenter, Analytical expressions for energies, degeneracies and critical temperatures of the 2d square and 3d cubic ising models, *Physica A: Statistical Mechanics and its Applications* **349**, 487 (2005).
- [33] E. E. Vogel, P. Vargas, G. Saravia, J. Valdes, A. J. Ramirez-Pastor, and P. M. Centres, Thermodynamics of small magnetic particles, *Entropy* **19**, 499 (2017).
- [34] K. De'Bell, A. MacIsaac, and J. Whitehead, Dipolar effects in magnetic thin films and quasi-two-dimensional systems, *Reviews of Modern Physics* **72**, 225 (2000).
- [35] USGS, <https://earthquake.usgs.gov/earthquakes/search/usgs> (2024).
- [36] C. Tsallis, *Introduction to nonextensive statistical mechanics: approaching a complex world*, Vol. 1 (Springer, 2009).
- [37] O. Sotolongo-Costa and A. Posadas, Fragment-asperity interaction model for earthquakes, *Physical review letters* **92**, 048501 (2004).
- [38] L. Onsager, Crystal statistics. i. a two-dimensional model with an order-disorder transition, *Physical Review* **65**, 117 (1944).